Vibrational coupling in plasmonic molecules

Chongyue Yi[a], Pratiksha D. Dongare[b,c], Man-Nung Su[a], Wenxiao Wang[c], Debadi Chakraborty[d], Fangfang Wen[a], Wei-Shun Chang[a], John E. Sader[d], Peter Nordlander[c,e,f], Naomi J. Halas[a,c,e,f], and Stephan Link[a,c,f,1]

[a]Department of Chemistry, Rice University, Houston, TX 77005; [b]Applied Physics Graduate Program, Rice University, Houston, TX 77005; [c]Department of Electrical and Computer Engineering, Rice University, Houston, TX 77005; [d]ARC Centre of Excellence in Exciton Science, School of Mathematics and Statistics, The University of Melbourne, Parkville, VIC 3010, Australia; [e]Department of Physics and Astronomy, Rice University, Houston, TX 77005; and [f]Laboratory for Nanophotonics, Rice University, Houston, TX 77005

Edited by George C. Schatz, Northwestern University, Evanston, IL, and approved September 18, 2017 (received for review July 12, 2017)

Plasmon hybridization theory, inspired by molecular orbital theory, has been extremely successful in describing the near-field coupling in clusters of plasmonic nanoparticles, also known as plasmonic molecules. However, the vibrational modes of plasmonic molecules have been virtually unexplored. By designing precisely configured plasmonic molecules of varying complexity and probing them at the individual plasmonic molecule level, intramolecular coupling of acoustic modes, mediated by the underlying substrate, is observed. The strength of this coupling can be manipulated through the configuration of the plasmonic molecules. Surprisingly, classical continuum elastic theory fails to account for the experimental trends, which are well described by a simple coupled oscillator picture that assumes the vibrational coupling is mediated by coherent phonons with low energies. These findings provide a route to the systematic optical control of the gigahertz response of metallic nanostructures, opening the door to new optomechanical device strategies.

plasmonics | coherent phonon | ultrafast spectroscopy | optomechanics

Intermolecular and intramolecular energy transfer and redistribution, associated with many bond-selective reactions, are usually mediated by internal vibrational or rotational mode coupling (1–8). A coupled harmonic oscillator picture provides the simplest approximation to model vibrational interactions in molecules (9). When two vibrations are coupled, the result is a blueshift of the higher-frequency mode, while the lower-frequency mode is redshifted with a magnitude governed by the coupling strength (Fig. 1*A*). A quantum mechanical treatment becomes necessary to describe the more complex coupling in larger molecules that support many vibronic modes (10). As a consequence of quantum mechanical state mixing, unique spectroscopic features emerge, including frequency splitting and shifting, that can be exploited to deduce molecular structure through vibrational spectroscopy (10, 11). One such phenomenon is known as a Fermi resonance, which occurs when two energetically similar vibrations mix, resulting in frequency shifts and intensity redistribution of the uncoupled vibrational resonances (12). Often, one of the two interacting vibrational modes is an overtone, and coupling is maximized when $\omega_A = 2\omega_B$.

Many concepts of molecular spectroscopy have been successfully applied to clusters of proximal nanoparticles supporting plasmon resonances, known as plasmonic molecules. These include the hybridization of plasmons to form coupled modes due to strong near-field coupling, in analogy with molecular orbital theory (13, 14); the emergence of Fano interference (14–16); and the application of group theory to determine selection rules (17). The excitation of coherent lattice vibrations has also been observed through Raman spectroscopy (18, 19), ultrafast imaging (20, 21), and transient extinction spectroscopy (22–24). In this last method, the strong absorption of an ultrafast laser pulse by the plasmonic nanoparticle impulsively launches acoustic breathing modes that are detected optically with a time-delayed probe pulse (22, 25–27). The measured acoustic modes of isolated nanoparticles are well described by continuum elastic theory (22, 23, 28). However, vibrational coupling in plasmonic molecules has been virtually unexplored.

The few ultrafast studies on groupings of plasmonic nanoparticles have reported widely contradicting results. As the interparticle gap in gold nanodisk dimers was decreased from 212 to 7 nm, an increase in the oscillation period was measured and attributed to stronger near-field coupling (29). However, no change in vibration frequency was observed for gold nanocuboid dimers with varying separations (30, 31). In closely spaced dimers of gold nanospheres prepared by chemical methods, a second lower-frequency acoustic vibration was detected, corresponding to the stretching mode of a connected dumbbell (32). A similar stretching mode was seen in Raman measurements of nanosphere dimers that were mechanically coupled by surrounding polymer molecules, consistent with predictions based on continuum elastic theory (33, 34). By using individual nanostructure building blocks with highly controlled geometries and precise interparticle spacings to create plasmonic molecules, these observed disparities could be resolved. This approach has yielded much current fundamental insight into the near-field interactions of plasmonic modes (13, 16, 25, 35), but has not been applied to the vibrations of plasmonic molecules.

Here, we report an experimental observation of vibrational coupling within plasmonic molecules, occurring through the acoustic modes of their constituent nanoparticles. We use transient extinction spectroscopy of individual plasmonic molecules with wavelength tunable optical probe pulses that detected specific acoustic modes in the metal nanoparticles launched impulsively through ultrafast laser excitation. The precise control of size, spacing, and arrangement of the individual nanoparticle constituents of each plasmonic molecule is accomplished by using electron-beam lithographic fabrication, allowing us to tune and control the coupling strength. These results demonstrate the breakdown of classical continuum elastic theory and suggest that coherent phonons of the substrate play an important role in the acoustic mode coupling in these systems.

We chose to study a decamer of plasmonic nanodisks, where a larger central disk is surrounded by an outer ring of nine smaller disks. A schematic illustration of a decamer is shown in

Significance

In this work, we provide evidence of vibrational coupling between the constituent atoms in a plasmonic molecule mediated by coherent substrate phonons. A simple coupled harmonic oscillator model provides fundamental insight into the optomechanical selection rules for the launching of vibrational modes. The coupling strength-dependent vibrational frequency shifts can be directly manipulated by precise tuning of the structure of the plasmonic molecule by using top-down lithography. This tunability paves the way for new strategies to design optomechanical devices based on metallic nanostructures.

Author contributions: C.Y., M.-N.S., W.-S.C., J.E.S., P.N., N.J.H., and S.L. designed research; C.Y., P.D.D., M.-N.S., D.C., F.W., and W.-S.C. performed research; C.Y., W.W., and D.C. analyzed data; and C.Y., W.-S.C., J.E.S., P.N., N.J.H., and S.L. wrote the paper.

The authors declare no conflict of interest.

This article is a PNAS Direct Submission.

[1]To whom correspondence should be addressed. Email: slink@rice.edu.

This article contains supporting information online at www.pnas.org/lookup/suppl/doi:10.1073/pnas.1712418114/-/DCSupplemental.

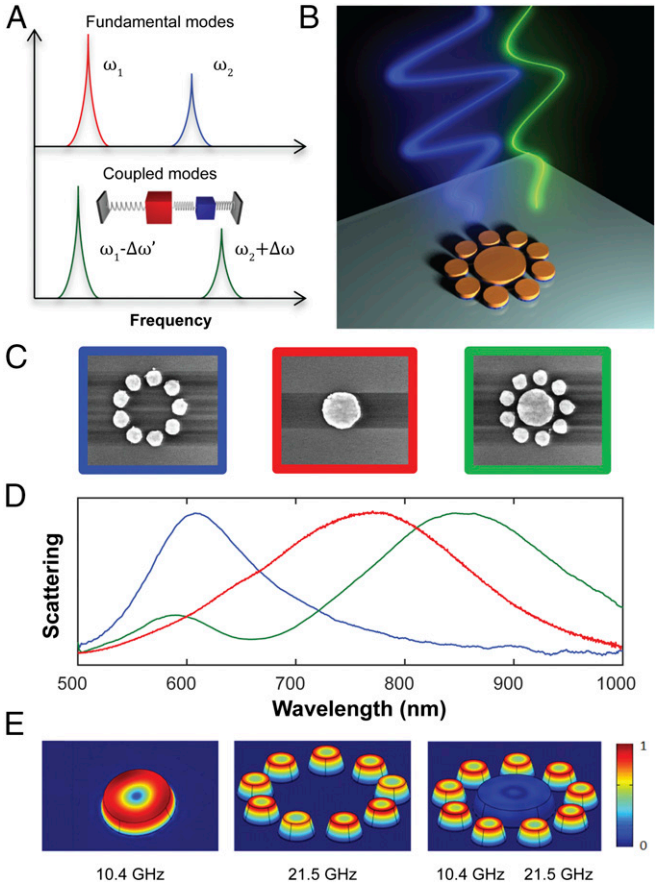

Fig. 1. Illustration of coupled acoustic modes and characterization of a gold decamer. (*A*) Frequency domain representation of two fundamental modes and the resulting shifts due to coupling. (*B*) Schematic representation of a gold nanodisk cluster. Gold nanodisks with a 35-nm thickness are fabricated on top of a 2-nm Ti adhesion layer and evaporated onto a glass substrate by using electron-beam lithography. Pump (blue) and probe (green) pulses are collinearly focused on a single cluster by passing through the same objective. (*C*) SEM images of the decamer (green) and its components: central disk (red) and outer ring (blue). The size of each image is 640 × 550 nm. (*D*) Corresponding spectra obtained by dark-field scattering spectroscopy (*Materials and Methods*). The central disk has a diameter of 178 nm, while the disks of the outer ring measure 78 nm with a constant gap size of 20 nm between the central disk and the outer ring. The gap size between the 78-nm nanodisks is 23 nm. (*E*) Simulations of the displacement fields of the central disk (*Left*; 10.4 GHz), outer ring (*Center*; 21.5 GHz), and decamer (*Right*; 10.4 and 21.5 GHz) performed by using FEM modeling.

Fig. 1*B*, together with blue femtosecond pump and wavelength-tunable probe pulses. A variety of decamers, as well as their components—central disks, outer rings, homodimers, and heterodimers—are fabricated (*Materials and Methods* and Fig. 1*C*). The nanodisks are not in mechanical contact except through the supporting glass substrate.

Near-field coupling in the decamer leads to a Fano resonance near 650 nm in the dark-field scattering spectrum (Fig. 1*D*). Simulated scattering spectra are provided in *SI Appendix*, Fig. S2. Based on plasmon hybridization theory (13), this Fano resonance can be attributed to the interference between a broad superradiant mode, where the plasmons of all nanodisks oscillate in phase, and a narrow subradiant mode, where the plasmon oscillations of the central disk and outer ring are out of phase (14, 16). In contrast, the scattering spectra of the 178-nm central disk and the outer ring of 78-nm disks have a single plasmon resonance peaked at 780 and 600 nm, respectively.

Based on finite element method (FEM) analysis of the acoustic vibrations of the decamer, including the substrate and all acoustic modes supported by this system when considering continuum elastic theory, no frequency shifts should be expected for the modes corresponding to the isolated central disk and outer ring (Fig. 1*E*). It is important to also note that the experimental in-plane breathing frequency of different-diameter gold nanodisks (i.e., plasmonic atoms) is quantitatively reproduced with continuum elastic theory (*SI Appendix*, Fig. S3).

Through transient extinction spectroscopy (*Materials and Methods* and *SI Appendix*, Fig. S1), clear shifts of the fundamental frequencies corresponding to the larger central disk and smaller ring disks are observed (Fig. 2). An individual central disk (Fig. 2*A*), outer ring (Fig. 2*B*), and decamer (Fig. 2*C*) are excited above the gold interband transition at 405 nm and probed with 810-nm pulses that spectrally overlapped the plasmon resonances of each nanostructure. All transient transmissions show a fast initial rise, due to ultrafast bleaching caused by the excitation pulse, followed by a few-picosecond decay due to electron–phonon coupling (22, 36). Thermalization of the hot lattice with the surrounding medium occurs on a timescale of several hundred picoseconds. This slower decay component is modulated by the periodic lattice expansion of excited acoustic breathing modes that modify the plasmon resonance. By subtracting the contributions from electron–phonon and phonon–phonon coupling, the acoustic modes are isolated (Fig. 2 *A*–*C*, *Lower*) and obey damped harmonic oscillations, yielding vibration frequencies of 10.7 ± 0.8 and 21.5 ± 0.8 GHz for the central disk and outer ring, respectively (see *SI Appendix* for details). Considering the absence of frequency shifts in the FEM simulations of these structures (Fig. 1*E*) and the fact that continuum elastic theory has not previously failed to describe the mechanical properties of individual metallic nanoparticles (34, 37–40), the corresponding modes in the decamer are unexpectedly shifted to 10.4 ± 0.7 and 24.7 ± 0.4 GHz. In particular, the blueshift of the higher-frequency mode is found to be well outside the measurement error, as confirmed with fast Fourier transform (FFT) analysis (Fig. 2*D*). It is important to note that the FEM calculations in Fig. 1*E* are carried out by using full 3D continuum elastic simulations that intrinsically accounted for all classical phenomena, such as surface acoustic waves, acoustic radiation damping, and coupling. The disagreement with experiments, as illustrated further below, points to a breakdown of continuum elastic theory.

The interrogation of individual structures, as performed here, ensures that the transmission oscillation lifetimes are not masked by inhomogeneous effects, because intrinsic damping rates can vary tremendously for lithographically prepared samples, even for extraordinarily small size variations (24, 37). Tuning the probe wavelength from the fundamental laser line at 810 to 650 nm by generating a white-light continuum followed by spectral windowing (*Materials and Methods* and *SI Appendix*, Fig. S1) allows us to isolate only the higher-frequency acoustic mode in the decamer and its components (Fig. 2 *E*–*G*). Although the oscillation frequency and damping time are independent of probe wavelength, the oscillation amplitude exhibits a strong probe wavelength dependence: probing closer to the plasmon resonance maximum results in a larger amplitude. The 3.2-GHz blueshift is well reproduced with the 650-nm probe (Fig. 2*H*).

To address whether the observed mechanical coupling is specific to the decamer structure and its Fano resonance, we investigate simpler plasmonic molecules: homodimers and heterodimers. Homodimers consisting of two 78- and 178-nm-diameter disks, as well as the heterodimer composed of one small and one large nanodisk, do not support a Fano resonance in their scattering spectra (*SI Appendix*, Fig. S4). Although heterodimers can support Fano resonances (41), in our case, the plasmon modes of the two nanodisks are sufficiently detuned. For the homodimer consisting of two 178-nm-diameter disks, no frequency shift is detected relative to that of the individual disk (Fig. 3 *A* and *B*), and likewise for the smaller

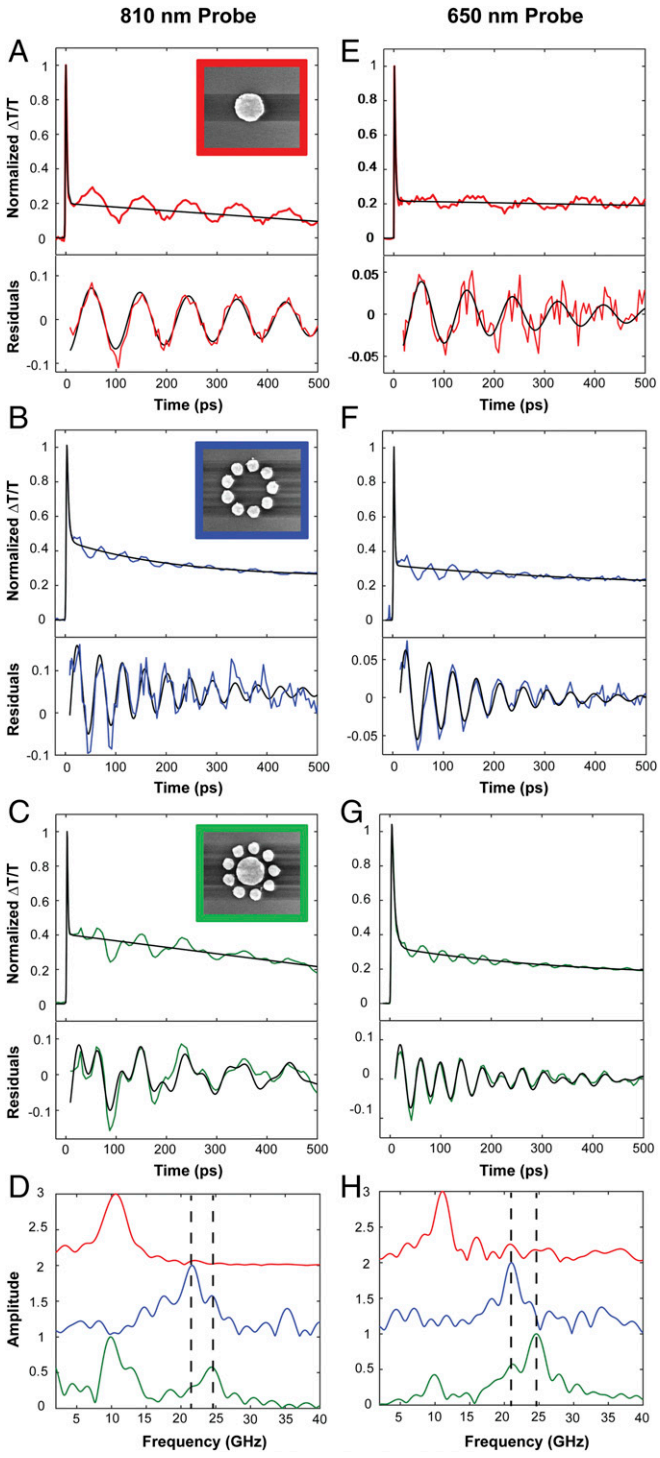

Fig. 2. Transient transmission of a decamer and its components. Transient transmission of a central disk (*A* and *E*), an outer ring (*B* and *F*), and a decamer (*C* and *G*) excited by 405-nm laser pulses, probed at 810 nm (*A*–*C*) or 650 nm (*E*–*G*). Acoustic modes are isolated by first subtracting the response corresponding to electron–phonon and phonon–phonon coupling and then describing the residuals by damped harmonic oscillations. Acoustic frequencies of 10.7 ± 0.8 GHz for the central disk and 21.5 ± 0.8 GHz for the outer ring are obtained, while the frequencies of the decamer are 10.4 ± 0.7 and 24.7 ± 0.4 GHz. Black lines in all figures indicate fits to the model described in *Materials and Methods*. The SEM images of each structure are shown as *Insets* in *A*–*C*. The SEM image size is 640 × 550 nm. (*D* and *H*) FFT analysis of the experimentally obtained acoustic modes.

homodimer and its constituent 78-nm disk (Fig. 3 *C* and *D*). The smaller nanodisk-based structures are probed at 650 nm to better resolve their weaker oscillations. In fact, we find the same vibration frequency of 21.8 GHz for an individual 78-nm disk, its homodimer, and rings made from different numbers of this size nanodisk with varying gap sizes (Fig. 2 *B* and *F* and *SI Appendix*, Figs. S5–S8).

However, for the heterodimer, the same-magnitude frequency shift is observed (Fig. 3 *C* and *D*) as for the decamer (Fig. 2 *D* and *H*). With a 650-nm probe, we detect two oscillation periods of similar magnitudes, corresponding to the larger 178-nm and smaller 78-nm disk (Fig. 3*C*). The frequency of the latter is blueshifted by 3.3 GHz compared with an individual 78-nm disk (Fig. 3*D*). This observation clearly indicates that the measured frequency shifts are not unique to the decamer geometry, but are also present in simpler plasmonic molecules. These data also indicate that size (mass) mismatch of the individual constituents in plasmonic molecules is likely to give rise to this coupling of optically excited phonons. The advantage of investigating the decamer is an increased signal, improving our ability to reliably determine small frequency shifts.

Further control experiments and simulations allow us to exclude electromagnetic near-field coupling as a possible mechanism for the measured shifts in acoustic frequencies. No change in vibration frequency is seen for both the homodimer and heterodimer when the probe beam polarization is switched from parallel to perpendicular with respect to the main dimer axis (*SI Appendix*, Figs. S9 and S10). Electromagnetic coupling is strongest in dimers for parallel polarization (25, 35). Boundary element method (BEM) (42) simulations of the extinction spectra for different clusters of nanospheres undergoing periodic lattice expansions yields no evidence that the changes in the measured transient transmissions could be simply explained by optomechanically modified plasmon coupling (*SI Appendix*, Figs. S11 and S12). The experimental acoustic frequencies are furthermore independent of the pump and probe laser powers (*SI Appendix*, Figs. S13 and S14).

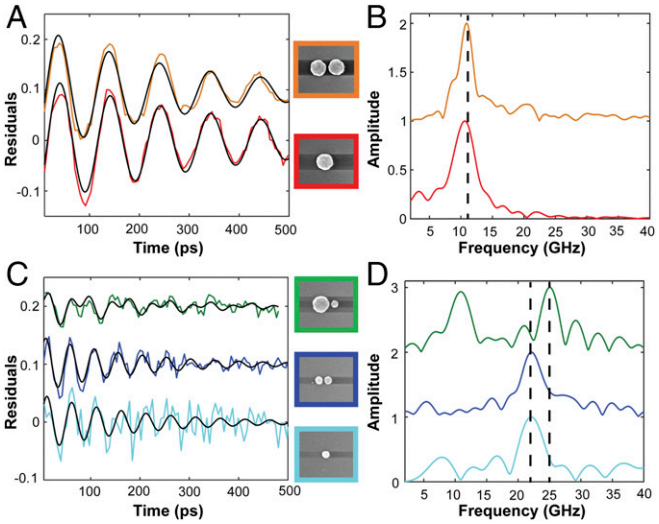

Fig. 3. Vibrational coupling in nanodisk dimers. (*A*) Time-resolved acoustic mode vibrations of a single 178-nm-diameter gold nanodisk (red) and its homodimer (orange) recorded at a probe wavelength of 810 nm. (*B*) FFT analysis reveals no frequency shift. (*C*) Time-resolved acoustic mode vibrations of a single 78-nm-diameter gold nanodisk (light blue) and its homodimer (dark blue) compared with a heterodimer (green) consisting of a larger 178-nm and a smaller 78-nm disk recorded with a 650-nm probe wavelength. (*D*) FFT analysis shows a blueshift of the high-frequency mode of the heterodimer, while for a homodimer the frequency is not shifted. The dimer gap is 20 nm. The SEM images of the structures are shown in the center of the figure. The size of each SEM image is 640 × 550 nm.

A coupled mechanical oscillator model (*SI Appendix*, Fig. S15) can explain the main experimental observations. The acoustic frequency of each individual nanodisk depends inversely on its diameter (22, 37). Connecting two oscillating nanodisks by a spring creates two new coupled acoustic modes (43). In general, one coupled mode blueshifts, while the other redshifts. For the special case of a homodimer with degenerate frequencies, the in-phase coupled oscillation undergoes no frequency shift, while a blueshift is expected for the out-of-phase oscillation (*SI Appendix*, Eq. **S13**). Experimentally, this blueshift is not observed, because the impulsive launching of acoustic vibrations by ultrafast laser heating only drives in-phase oscillations. This result gives us insight into the opto-mechanical selection rules for the launching of vibrational modes in plasmonic molecules. For the heterodimer, both coupled modes are allowed, and we indeed measure a blueshift of the higher-frequency and a redshift of the lower-frequency vibration. The latter frequency shift is much smaller and barely detectable within experimental uncertainties. However, based on our coupled oscillator model and estimating the coupling strength from the blueshift of the higher-frequency mode, we calculate a redshift of 0.25 GHz, in agreement with our measurements for both the heterodimer and the decamer.

Precise control over the geometry of our plasmonic molecules allows us to further characterize the vibrational coupling in nanodisk assemblies, revealing a strong gap size dependence. In the decamer structure, we investigate the degree of blueshift for the acoustic vibrations of the ring nanodisks as we change the interparticle separation from 15 to 50 nm between the central disk and outer ring (Fig. 4 *A*–*C*; see *SI Appendix*, Fig. S16 for the corresponding scattering spectra). The coupled acoustic mode in these plasmonic molecules clearly exhibits a continuous redshift toward the fundamental frequency of the 78-nm nanodisk with increasing interparticle separation (Fig. 4 *A* and *B*). This trend can be quantitatively accounted for with our coupled harmonic oscillator model by assuming that the vibrational coupling is mediated by coherent phonons of the substrate. These phonons are excited by a nanodisk vibration and propagate with an intensity (deformation amplitude) proportional to (44, 45):

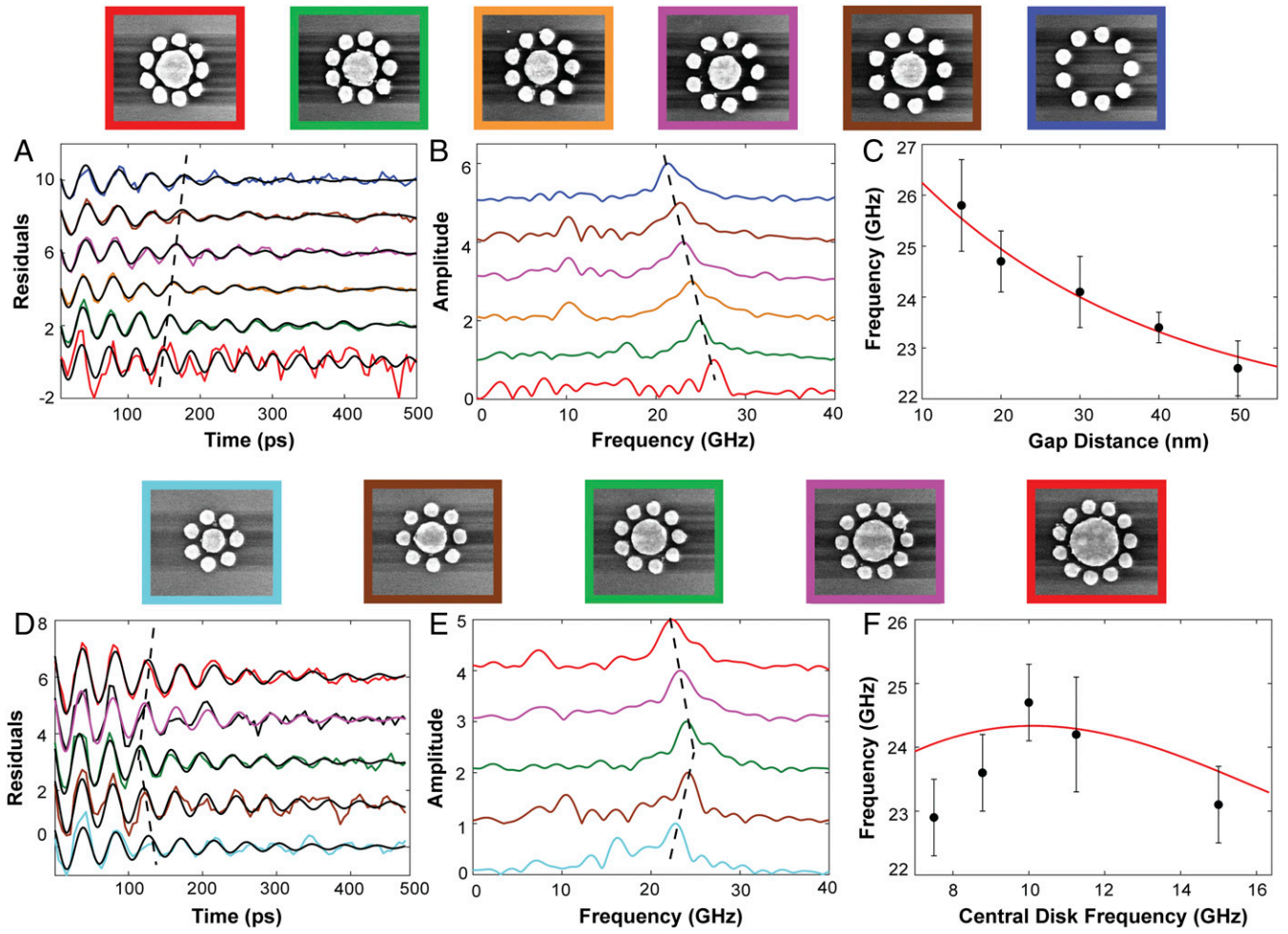

Fig. 4. Geometry-dependent vibrational coupling in nanodisk clusters. (*A*) Time-resolved acoustic mode vibrations for individual decamers with different gap sizes. The gap between the central disk and the outer ring is increased from 15 nm (red) to 20 nm (green), 30 nm (orange), 40 nm (magenta), and 50 nm (brown) and compared with the outer ring only (blue). Other structural parameters are kept the same as in Figs. 1 and 2. (*B*) Corresponding FFT analysis of *A*. (*C*) Measured acoustic frequencies as a function of gap size. The red line is a fit to Eq. **2** using for ω the value measured for the larger nanodisk that is driving the interaction. (*D*) Time-resolved acoustic mode vibrations for individual decamers having central disks with sizes of 250 nm (red), 205 nm (magenta), 178 nm (green), 160 nm (brown), and 120 nm (sky blue). The disks in the outer ring have a diameter of 78 nm. The interparticle gap between the central disk and outer ring is held constant at 20 nm. (*E*) Corresponding FFT analysis of *D*. (*F*) Measured acoustic frequency as a function of the central disk frequency that is independently determined for each size. The red curve plots Eq. **2** using the value for α obtained from the gap size dependence in *C* without any further adjustments. The probe wavelength is 650 nm for all measurements. All SEM images correspond to a size of 640 × 550 nm.

$$I(\omega, d) = \beta e^{-\alpha\omega^{\eta} d} \quad [1]$$

where I is the local deformation amplitude, β is the initial vibration amplitude, α is the attenuation coefficient, d is the propagation distance, and ω is the phonon frequency. The nonnegative materials parameter η has a value of 2 (46). When this lattice deformation reaches the other disk, its effect on this disk's acoustic vibration (described by a force constant, k) is equivalent to a disk–disk coupling constant $k_3 \propto kI(\omega, d) \propto \omega^2 I(\omega, d)$. With the initial vibrational amplitude of the disk being inversely proportional to the vibrational frequency $\beta \propto \omega^{-1}$, the effective phonon-mediated coupling between the disks depends on both frequency and separation as:

$$k_3 \propto \omega e^{-\alpha\omega^2 d}. \quad [2]$$

The measured gap size-dependent frequency shift is fully accounted for by using this expression (Fig. 4*C*). A gap-size dependence for the outer ring in isolation produces no frequency shift (*SI Appendix*, Fig. S8), consistent with our results for homodimers (Fig. 3). From these results, we conclude that the coupling medium for the acoustic breathing modes of the nanodisks must be the supporting substrate, leading us to investigate the substrate dependence of the vibrational coupling for decamers (*SI Appendix*, Fig. S17). When comparing the glass substrate with stiffer Al_2O_3, we find a smaller blueshift of 1.6 GHz for the high-frequency mode of the nanodisks in the outer ring, suggesting weaker coupling due to a smaller vibration amplitude β, which is determined by the Young's modulus of the substrate (47). Interestingly, the optically launched vibrational coupling is entirely unaffected by the Ti adhesion layer between the nanodisks and the glass substrate (*SI Appendix*, Fig. S18). Adding water as a medium between the nanodisks also has no effect, apart from reducing the damping time (*SI Appendix*, Fig. S19). Although we expect that FEM simulations should describe these systems well, including the measured frequency shifts, the departure from the classical continuum elastic theory could be caused by the combination of low-energy acoustic modes and the nature of the substrate, which in every case was noncrystalline material. It has been reported that in glasses the Debye approximation for acoustic modes in the millielectronvolts to submillielectronvolts range fails as their wavelength becomes comparable to the local disorder (48). More experiments and modeling are, however, needed to further investigate this observed phenomenon.

We now turn to the frequency dependence of the vibrational coupling in plasmonic molecules. Fig. 4 *D*–*F* shows the time-resolved acoustic mode vibrations for decamers with varying diameters of their central disks (see *SI Appendix*, Fig. S20 for the corresponding scattering spectra). When increasing the central disk from 120 to 178 nm, we measure an increasing blueshift for the coupled mode. However, a further size increase leads to smaller frequencies. This behavior is qualitatively reproduced by our coupled oscillator model (Fig. 4*F*) by using the coupling constant from Eq. **2** and the gap size-dependent results from Fig. 4*C* without any further adjustable parameters. Because the central disk has a larger absolute vibration amplitude, we assume that the central disk is driving vibrational coupling. Interestingly, the maximum measured frequency shift in Fig. 4*F* is for the 178-nm central disk with a frequency of 10.7 GHz, a value very close to one-half of the fundamental mode frequency (21.5 GHz) for the 78-nm outer ring disks. This result may indicate the appearance of a Fermi resonance, similar to molecular systems (12, 49). The interaction of the first overtone of the central disk with the fundamental mode of the ring disks may result in an avoided crossing. Although overtones are not observed in the present transient extinction measurements, both ultrafast X-ray diffraction imaging and molecular dynamics simulations have revealed the presence of higher-order acoustic vibrations in gold nanoparticles (20, 50). Detuning the central disk frequency from the resonance condition of $\hbar\omega_{\text{ring}} = \hbar\omega_{\text{overtone}} = 2\hbar\omega_{\text{central disk}}$ results in weaker coupling, and therefore smaller frequency shifts.

In summary, the vibrational coupling of acoustic modes in plasmonic molecules has been observed. While classical continuum elastic theory describes the acoustic modes of the individual nanostructure components very well, it fails to account for the observed acoustic mode coupling, likely because of their low energies. The coupling instead follows a coherent phonon model, mediated by the supporting substrate and controllably tuned by varying the distance between the individual constituent nanoparticles of the plasmonic molecules. Coupling-induced frequency shifts are only detected in clusters composed of nanodisks with differing sizes, providing insight into the selection rules for excitation of these vibrational modes. These results show that tunability and control of the mechanical properties through a limited set of geometrical parameters can be achieved and could provide new strategies for nonlinear photoacoustic imaging, Fabry–Perot type optical cavities, devices based on optomechanically induced transparency, and families of new gigahertz microelectromechanical systems with optical excitation and/or readout.

Materials and Methods

Sample Preparation. Individual and coupled gold nanodisks are fabricated on a glass substrate by using electron-beam lithography. The substrates are sonicated in acetone for 5 min, rinsed with isopropyl alcohol, cleaned with oxygen plasma for 5 min, and spin-coated with a layer of polymethyl methacrylate resist (PMMA 950 A2; MicroChem) and Espacer 300Z (Showa Denko). Electron-beam patterning of the resist is performed by using a FEI QUANTA 650 SEM with a voltage of 30 K and a beam current of 40 pA. The resist is then developed in a 1:3 methyl isobutyl ketone:IPA solution. Titanium adhesion and gold layers are deposited on the substrates by electron-beam evaporation. The thickness of the deposited metals is monitored by a quartz crystal microbalance and further confirmed by AFM measurements. The structures are treated with a standard lift-off process via incubation in *N*-methyl-2-pyrrolidone at 65 °C for 2 h.

Dark-Field Scattering Spectroscopy. Scattering spectra of individual nanostructures are measured by using a dark-field spectroscopy setup based on an inverted microscope (Zeiss Axio Observer m1). White light from a halogen lamp is focused on the sample by a dark-field condenser [Zeiss, numerical aperture (N.A.) = 1.4], and the scattered signals are collected by a 74 × reflective objective (Beck Optronic Solutions; N.A. = 0.65) and directed into a spectrograph (Princeton Instruments Acton SP2150) toward a charge-coupled device camera (Princeton Instruments Pixis 400BR). The spectrum is obtained by dividing the collected signal by the white light spectrum after subtracting background.

Single-Particle Transient Extinction Spectroscopy. A diode-pumped laser (Coherent Verdi) is used to pump a Ti-Sapphire oscillator (KMLab Griffin) to generate a 810-nm beam with a pulse duration of ∼80 fs. The 405-nm pump beam is generated by frequency-doubling part of the 810-nm fundamental beam in a beta barium borate crystal (Altos BBO-1004H). The other part of the 810-nm femtosecond beam is focused into a photonic crystal fiber (Newport SCG-800) to generate a supercontinuum white light. By using 25-nm bandpass filters, specific wavelengths are selected as probe. The probe beam passes through an optical delay line (Newport UTS150CC), and the intensity of the pump beam is modulated by an acousto-optic modulator (IntraAction AOM-402AF1) with a frequency of 720 kHz. The pump and probe beams are collinearly overlapped by a dichroic mirror before being focused onto the sample by the same objective (Zeiss; N.A. = 1.4). The pump (405 nm) and probe (810 or 650 nm) powers are 150 and 50 μW, respectively, unless mentioned specifically. The beam polarizations are manipulated with half-wave plates positioned before the dichroic mirror that combines pump and probe beams. A parallel configuration of linearly polarized pump and probe beams is used. The diameter (FWHM) of both pump and probe beams is ∼400 nm, ensuring that the entire nanostructure is probed. While this condition is still met for the Fano clusters, the homodimers and heterodimers are all significantly smaller than the focused femtosecond laser pulses. The pump and probe beams are collected by a second objective (Zeiss; N.A. = 0.6) in a transmission geometry and passed through a 450-nm long-pass filter so that only the probe beam is detected by a photodiode. The signal is fed into a lock-in amplifier and connected to a counterboard (National

Instruments). Transient extinction images, used to locate individual nanodisks, are obtained with pump and probe beams overlapped temporarily by scanning the sample through the focused laser beams using a piezo scanning stage (Physik Intrumente P-517.3CL). Time transients are acquired by moving the optical delay line and repeated at least two times to ensure the reproducibility of each measurement and photostability of the sample.

Finite Element Method Simulations. The 3D gold nanoclusters, as shown in Fig. 1*C*, are modeled in the commercial finite element software COMSOL Multiphysics by using its frequency response solver for a solid. For numerical simulations, the interaction between the gold nanodisk with the 2-nm Ti adhension layer and the glass substrate is considered. To truncate the thickness of the thicker glass layer, a perfectly matched layer (PML) on the bottom of the glass substrate is used to absorb propagating acoustic waves. The dimensions of the glass layer and the PML are optimized by considering different thicknesses and radii of these layers. The reported results are independent of mesh size to within 0.1%. We consider three different cases: a 178-nm central disk, a ring composed of nine 78-nm nanodisks, and a decamer. The deformation field of the central disk, outer ring, and decamer with a gap size of 20 nm is shown in Fig. 1*E*. The simulated frequencies do not change as the central disk is inserted into the ring and are also independent of the gap size, as we vary it from 5 to 20, 44, and 88 nm.

BEM Simulations. Simulations of the extinction and scattering spectra of the different gold nanostructures are performed with the BEM by using the MNPBEM toolbox implemented in the Matlab software. Gold nanostructures with a Ti adhesion layer on top of a glass substrate are considered. The dielectric function of gold is taken from Johnson and Christy (51), while values for Ti and glass are taken from Palik and Ghosh (52). The geometry of each nanostructure is adopted from the SEM images.

Associated Content. *SI Appendix* provides experimental details and results, including the setup of the transient extinction microscope, scattering spectra of decamers and outer rings with different configurations, size-dependent vibrations of individual nanodisks, acoustic vibrations of outer rings with different gap sizes and different numbers of containing nanodisks, probe polarization-dependent vibration of dimers, power-dependent vibrations of decamers, coupled oscillator analysis, and environment-dependent vibration of decamers. For a complete overview, all measured acoustic frequencies and damping times are provided in *SI Appendix*, Tables S1–S4.

ACKNOWLEDGMENTS. This work was supported by Robert A. Welch Foundation Grants C-1222 (to P.N.), C-1220 (to N.J.H.), and C-1664 (to S.L.). P.N., N.J.H., and S.L. were supported by Army Grant MURI W911NF-12-1-0407 and Air Force Grant MURI FA9550-15-1-0022. S.L. was supported by National Science Foundation Grant ECCS-1608917. D.C. and J.E.S. were supported by the Australian Research Council (ARC) grants scheme and the ARC Centre of Excellence in Exciton Science.

1. Pascual JI, Lorente N, Song Z, Conrad H, Rust HP (2003) Selectivity in vibrationally mediated single-molecule chemistry. *Nature* 423:525–528.
2. Backus EHG, Eichler A, Kleyn AW, Bonn M (2005) Real-time observation of molecular motion on a surface. *Science* 310:1790–1793.
3. Killelea DR, Campbell VL, Shuman NS, Utz AL (2008) Bond-selective control of a heterogeneously catalyzed reaction. *Science* 319:790–793.
4. Bartels L, Wang F, Möller D, Knoesel E, Heinz TF (2004) Real-space observation of molecular motion induced by femtosecond laser pulses. *Science* 305:648–651.
5. Komeda T, Kim Y, Kawai M, Persson BNJ, Ueba H (2002) Lateral hopping of molecules induced by excitation of internal vibration mode. *Science* 295:2055–2058.
6. Wang Z, Pakoulev A, Dlott DD (2002) Watching vibrational energy transfer in liquids with atomic spatial resolution. *Science* 296:2201–2203.
7. Woutersen S, Bakker HJ (1999) Resonant intermolecular transfer of vibrational energy in liquid water. *Nature* 402:507–509.
8. Huang Y, Rettner CT, Auerbach DJ, Wodtke AM (2000) Vibrational promotion of electron transfer. *Science* 290:111–114.
9. Slater NB (1959) *Theory of Unimolecular Reactions* (Cornell Univ Press, Ithaca, NY).
10. Wilson EB, Decius JC, Cross PC (1980) *Molecular Vibrations: The Theory of Infrared and Raman Vibrational Spectra* (Dover, New York).
11. Preston TC, Signorell R (2011) Vibron and phonon hybridization in dielectric nanostructures. *Proc Natl Acad Sci USA* 108:5532–5536.
12. Fermi E (1931) Über den ramaneffekt des kohlendioxyds. *Z Phys* 71:250–259.
13. Prodan E, Radloff C, Halas NJ, Nordlander P (2003) A hybridization model for the plasmon response of complex nanostructures. *Science* 302:419–422.
14. Fan JA, et al. (2010) Self-assembled plasmonic nanoparticle clusters. *Science* 328:1135–1138.
15. Zhang Y, Wen F, Zhen YR, Nordlander P, Halas NJ (2013) Coherent Fano resonances in a plasmonic nanocluster enhance optical four-wave mixing. *Proc Natl Acad Sci USA* 110:9215–9219.
16. Luk'yanchuk B, et al. (2010) The Fano resonance in plasmonic nanostructures and metamaterials. *Nat Mater* 9:707–715.
17. Jain PK, Ghosh D, Baer R, Rabani E, Alivisatos AP (2012) Near-field manipulation of spectroscopic selection rules on the nanoscale. *Proc Natl Acad Sci USA* 109:8016–8019.
18. Wheaton S, Gelfand RM, Gordon R (2015) Probing the Raman-active acoustic vibrations of nanoparticles with extraordinary spectral resolution. *Nat Photonics* 9:68–72.
19. Portales H, et al. (2008) Probing atomic ordering and multiple twinning in metal nanocrystals through their vibrations. *Proc Natl Acad Sci USA* 105:14784–14789.
20. Clark JN, et al. (2013) Ultrafast three-dimensional imaging of lattice dynamics in individual gold nanocrystals. *Science* 341:56–59.
21. Valley DT, Ferry VE, Flannigan DJ (2016) Imaging intra- and interparticle acousto-plasmonic vibrational dynamics with ultrafast electron microscopy. *Nano Lett* 16:7302–7308.
22. Hartland GV (2011) Optical studies of dynamics in noble metal nanostructures. *Chem Rev* 111:3858–3887.
23. Pelton M, et al. (2009) Damping of acoustic vibrations in gold nanoparticles. *Nat Nanotechnol* 4:492–495.
24. Su MN, et al. (2017) Optomechanics of single aluminum nanodisks. *Nano Lett* 17:2575–2583.
25. Schumacher T, et al. (2011) Nanoantenna-enhanced ultrafast nonlinear spectroscopy of a single gold nanoparticle. *Nat Commun* 2:333.
26. O'Brien K, et al. (2014) Ultrafast acousto-plasmonic control and sensing in complex nanostructures. *Nat Commun* 5:4042.
27. Dowgiallo AM, Schwartzberg AM, Knappenberger KL (2011) Structure-dependent coherent acoustic vibrations of hollow gold nanospheres. *Nano Lett* 11:3258–3262.
28. Yu K, Zijlstra P, Sader JE, Xu QH, Orrit M (2013) Damping of acoustic vibrations of immobilized single gold nanorods in different environments. *Nano Lett* 13:2710–2716.
29. Huang W, Qian W, Jain PK, El-Sayed MA (2007) The effect of plasmon field on the coherent lattice phonon oscillation in electron-beam fabricated gold nanoparticle pairs. *Nano Lett* 7:3227–3234.
30. Wang L, Nishijima Y, Ueno K, Misawa H, Tamai N (2009) Near-IR vibrational dynamics of periodic gold single and pair nanocuboids. *Appl Phys Lett* 95:053116.
31. Wang L, Nishijima Y, Ueno K, Misawa H, Tamai N (2012) Effect of dipole coupling on near-IR LSPR and coherent phonon vibration of periodic gold pair nanocuboids. *J Phys Chem C* 116:17838–17846.
32. Tchebotareva AL, et al. (2009) Acoustic and optical modes of single dumbbells of gold nanoparticles. *ChemPhysChem* 10:111–114.
33. Girard A, et al. (2016) Mechanical coupling in gold nanoparticles supermolecules revealed by plasmon-enhanced ultralow frequency Raman spectroscopy. *Nano Lett* 16:3843–3849.
34. Saviot L, Murray DB (2010) Vibrations of weakly coupled nanoparticles. *Phys Rev B* 81:235432.
35. Halas NJ, Lal S, Chang WS, Link S, Nordlander P (2011) Plasmons in strongly coupled metallic nanostructures. *Chem Rev* 111:3913–3961.
36. Harutyunyan H, et al. (2015) Anomalous ultrafast dynamics of hot plasmonic electrons in nanostructures with hot spots. *Nat Nanotechnol* 10:770–774.
37. Chang WS, et al. (2015) Tuning the acoustic frequency of a gold nanodisk through its adhesion layer. *Nat Commun* 6:7022.
38. Chakraborty D, van Leeuwen E, Pelton M, Sader JE (2013) Vibration of nanoparticles in viscous fluids. *J Phys Chem C* 117:8536–8544.
39. Lethiec CM, Madison LR, Schatz GC (2016) Dependence of plasmon energies on the acoustic normal modes of Ag-n (n=20, 84, and 120) clusters. *J Phys Chem C* 120:20572–20578.
40. Kirschner MS, et al. (2016) Size-dependent coherent-phonon plasmon modulation and deformation characterization in gold bipyramids and nanojavelins. *ACS Photonics* 3:758–763.
41. Brown LV, Sobhani H, Lassiter JB, Nordlander P, Halas NJ (2010) Heterodimers: Plasmonic properties of mismatched nanoparticle pairs. *ACS Nano* 4:819–832.
42. Waxenegger J, Trugler A, Hohenester U (2015) Plasmonics simulations with the mnpbem toolbox: Consideration of substrates and layer structures. *Comput Phys Commun* 193:138–150.
43. Okamoto H, et al. (2013) Coherent phonon manipulation in coupled mechanical resonators. *Nat Phys* 9:480–484.
44. Damen EPN, Dieleman DJ, Arts AFM, de Wijn HW (2001) Generation and propagation of coherent phonon beams. *Phys Rev B* 64:174303.
45. Szabo TL, Wu J (2000) A model for longitudinal and shear wave propagation in viscoelastic media. *J Acoust Soc Am* 107:2437–2446.
46. Baldi G, Giordano VM, Monaco G, Ruta B (2010) Sound attenuation at terahertz frequencies and the boson peak of vitreous silica. *Phys Rev Lett* 104:195501.
47. Landau LD, Lifshitz EM (1986) *Theory of Elasticity* (Pergamon, Oxford).
48. Monaco G, Giordano VM (2009) Breakdown of the Debye approximation for the acoustic modes with nanometric wavelengths in glasses. *Proc Natl Acad Sci USA* 106:3659–3663.
49. Amat G, Pimbert M (1965) On Fermi resonance in carbon dioxide. *J Mol Spectrosc* 16:278–290.
50. Kotaidis V, et al. (2012) Vibrational symmetry breaking of supported nanospheres. *Phys Rev B* 86:100101.
51. Johnson PB, Christy RW (1972) Optical constants of the noble metals. *Phys Rev B* 6:4370–4379.
52. Palik ED, Ghosh G (1998) *Handbook of Optical Constants of Solids* (Academic, San Diego).